Microstructural Evolution in Nimonic 263 for High Temperature Power Plant

S.A. Smith[1], G.D. West[1], K. Chi[2], W. Gamble[3] and R.C. Thomson[1]

[1]*Department of Materials,*
Loughborough University, Loughborough, LE11 3TU, UK

[2]*R&D Centre, Doosan Babcock, Porterfield Road, Renfrew, PA4 8DJ, UK*

[3]*E.ON Engineering Ltd, Technology Centre,*
Ratcliffe-on-Soar, Nottingham, NG11 0EE, UK

Abstract

It is necessary to develop and implement new power plant due to both current energy and environmental demands. To enable these objectives to be met, the next generation of power plant must be more efficient. A common method of improving efficiency in plant is to increase the steam temperatures and pressures, which will necessitate the introduction of new materials. Nickel-based alloys lend themselves to high temperature and pressure applications due to their significant creep strength and the ability to operate at metal temperatures above 750°C. Steam header and pipework systems carry steam from the boilers to the turbines and are of particular interest in this research. Header and pipework systems experience high operating temperatures and pressures in the power plant, and it is therefore paramount that a suitable material is chosen and methodologies are put in place to predict their safe operating lifetimes

Microstructural evolution in Nimonic 263, one candidate material for next generation plant, has been quantified using a variety of advanced analytical electron microscopy techniques, including field emission gun scanning electron microscopy (FEGSEM) and transmission electron microscopy (TEM). A focussed ion beam technique has also been used to produce site specific samples for examination in the TEM to assist in the identification of grain boundary precipitates.

The changes occurring in the microstructure as a result of time and temperature of exposure have been quantified and the precipitates fully identified. The results are also compared to predictions from thermodynamic equilibrium calculations. It is shown that variation in exposure time and temperature can affect the microstructural development, and therefore the mechanical properties, of the Nimonic 263 alloy.

1. Introduction

The development of new and existing high temperature materials is needed to enable the successful introduction of cleaner and more efficient next generation power plant. The need for their introduction can be attributed to current economics, environmental legislation and the ever increasing electricity demand. Increasing steam operating parameters is one way of achieving a more efficient plant; an increase from 540°C/180 bar to 700°C/300 bar is calculated to give an increase in steam turbine efficiency of approximately 13% [1]. To achieve this step change in operating parameters, new high temperature materials must be selected due to the inherent limitations in steels. Nimonic 263 is currently considered to be one of the leading candidate materials for use in high temperature applications in the next generation plant [1].

Nimonic 263 is a precipitation hardened Ni-Co-Cr based superalloy developed in 1960 by Rolls-Royce plc as a sheet material for use in gas turbines. It was originally developed with the intention of having the weld ductility and fabrication characteristics of Nimonic 75 and the creep rupture strength of Nimonic 80A [2]. The material is available in a variety of wrought (hot and cold worked) product forms, most commonly sheet used in a number of stationary applications in gas turbines such as combustion chambers, casings, liners, exhaust ducting and bearing housings [3]. Hot worked material in the form of thick section pipe as proposed for high temperature steam power plant will be the focus of this paper.

The status of Nimonic 263 as a candidate alloy is due to a wide range of desirable properties, including excellent elevated temperature strength, creep resistance, in addition to high corrosion and oxidation resistance [4]. Such properties are achievable due to a series of heat treatments and the high level of alloying in Nimonic 263. Nimonic 263 has an FCC austenitic (γ) matrix with the following phases reported to be present: gamma prime (γ') eta (η), MX, $M_{23}C_6$, M_6C and mu (μ) [5]. Precipitation of MX, $M_{23}C_6$ and γ' occur during the standard precipitation heat treatment. The precipitated γ' that forms is metastable and is replaced over time by the more stable η phase [6, 7].

The alloy has two main strengthening mechanisms; solid solution strengthening and precipitation hardening. Solution strengthening elements such as molybdenum provide high temperature strengthening through lattice distortion due to its atomic size difference from the matrix. Some of the benefits of solid solution strengthening include reduced diffusion and a lower overall stacking fault energy. Precipitation hardening is the principal strengthening mechanism in Nimonic 263 and occurs due to the precipitation of γ' during the precipitation hardening heat treatment (typically a few hours at 800°C). Initial precipitation creates a distribution of very fine spherical gamma prime particles.

This research details a microstructural study of the wrought alloy in the form of a thick section pipe, including the long term stability at exposure temperatures representative of likely plant conditions.

2. Materials and Experimental Procedure

The samples examined in this research were sourced from a forged thick section pipe of the following dimensions; 310 mm outside diameter, 170 mm bore diameter (resulting in a wall thickness of 70 mm) and 3140 mm length. The specific chemistry of the pipe was analysed in 3 locations showing overall very little change. The Al content did however vary from 0.31 wt.% in the bore to 0.37 wt.% in the outer diameter. The mean composition of the alloy used in this research is shown below in Table 1.

Table 1: Chemical composition of the Nimonic 263 (wt.%)

Element, wt.% (balance is Ni)							
C	Al	Co	Cr	Fe	Mo	Ti	N
0.06	0.33	19.89	20.41	0.45	5.85	2.11	0.006

Sections were cut from the pipe in order to produce a series of samples for metallurgical analysis. All samples have undergone a solution heat treatment (ST) of 1150°C for 2 hours, before being quenched to room temperature in water. The majority of the samples have also been subjected to a precipitation hardening heat treatment (PH) of 800°C for 4 hours. In addition samples of the precipitation hardened material were aged at a series of different temperatures and ageing times, as shown in Table 2.

Table 2: Ageing heat treatments

Ageing temperature (°C)	700°C	725°C	750°C
Ageing time (h)	8, 100, 1000, 3000, 10,000, 20,000	10000	8, 100, 1000

Samples were cut to a suitable size to be mounted, before a series of grinding stages were undertaken: 200, 600 and 1200 grit. Three separate polishing stages were then carried out for 12 minutes, polishing the samples with 9, 3, and 1 μm polishing solutions. The final preparation stage was a colloidal silica chemical polish of 0.04 μm for 20 minutes to highlight grain structure and remove any remaining fine scratches. The samples were then etched depending on the experimental technique being used; Fry's reagent (CuCl – 200 g, HCl – 1 l and water – 1 l) was used to highlight the gamma prime precipitates and Kallings no. 2 (CuCl$_2$ – 2 g, HCl – 40 ml and ethanol – 40-80 ml) was used to preferentially attack the grain boundaries and in turn reveal the alloy's grain structure.

Thermodynamic calculations were carried out using the mean chemical composition of Nimonic 263 to ascertain which phases were expected to be present at thermodynamic equilibrium and their amount through a temperature range of 400 - 1600°C. Calculations were extended to show the change in chemical composition of each phase with varied

temperature. The calculations were carried out using MTDATA[8], in conjunction with the Thermotech Ni-Data database[9].

Initial assessment of the alloy microstructure was carried out using both bright and dark field optical microscopy. Samples were analysed using a Reichert-Jung MeF3, inverted metallurgical microscope and images were collected using a Q-imaging Micropublisher 5.0 digital camera. Hardness testing was carried out on a Mitutoyo – AVK-C2 Vickers hardness testing unit, with a load of 10 kg applied for 10 s and an average of 10 readings taken for each sample.

A Carl Zeiss (Leo) 1530 VP field emission gun scanning electron microscope (FEGSEM) has been used in conjunction with a Pegasus combined electron backscatter diffraction (EBSD) and energy dispersive x-ray (EDX) system for both imaging and chemical analysis. The FEGSEM was operated in back scatter mode to distinguish between similar sized and shaped precipitates by utilising atomic number contrast. The SEM was operated in a voltage range of 5-20 kV and at a working distance between 3-15 mm, depending on the mode being used e.g. in-lens or electron back scatter.

Transmission electron microscopy (TEM) was used to study the grain boundary precipitates and their evolution as a result of heat treatment. Two different techniques were used to produce TEM specimens: both the 'in situ lift out' for thin foils and carbon extraction replication were used. The in-situ lift out technique was carried out using an fei Nova 600 Nanolab Dual Beam system. The technique involves finding a specific grain boundary or area of interest, depositing a layer of protective platinum and the ion beam is then used to mill a trench either side and thin the section between the two trenches. The thinned region is then removed using an Omniprobe manipulator and mounted onto a copper TEM grid and thinned to electron transparency. In the extraction replica technique, the samples were first etched in Kalling's before carbon was deposited using an Edwards carbon evaporator. The carbon replicas were then removed using an electrolytic etch consisting of 10% HCl in methanol at 5 V causing the carbon layer to break free from the substrate removing with it the second phases precipitates. The final stage was to collect the carbon replicas on a copper TEM grid. The resultant thin foils and replicas were analysed using a JEOL 2000FX TEM operated at 200 kV.

3. Results

3.1 Thermodynamic calculations

Thermodynamic calculations were carried out to predict the phase stability and the fraction of each phase present at equilibrium. The average composition from Table 1 was used to produce the thermodynamic phase calculations shown in Figures 1a and b. The calculations predicted the formation of the following six phases: gamma prime γ', gamma γ, MC and MX, Eta phase η, $M_{23}C_6$ and the Mu phase μ. Calculations were initially carried out allowing all phases to exist, and then subsequently with η phase suspended because it was known to be extremely slow to form, and therefore the latter calculation is expected to give a more realistic prediction for shorter ageing times and non equilibrium conditions. Each calculation predicted the formation of γ, γ', MX, $M_{23}C_6$ and Mu phase although the precipitation temperature and the fractions formed of each phase varied. The calculations predicted FCC γ as the bulk component or matrix of the alloy at a fraction of 0.84. The most significant difference between the two calculations was the predictions involving γ' precipitation. The calculation allowing of all phases, predicts γ' to form at 725°C and to be present at a fraction of 0.043 at 400°C. In the calculations with η suspended, γ' was found to form at 855°C and be present at a fraction of 0.058 at 400°C. Figures 1a and b show that the fraction of γ' decreases with an increase in temperature until dissolution. With η suspended, $M_{23}C_6$ was predicted to form at a reduced fraction; this may be due to the slightly higher Cr content in the increased fraction of γ' over the suspended η. The calculations also predicted the presence of MX and Mu phase in small quantities.
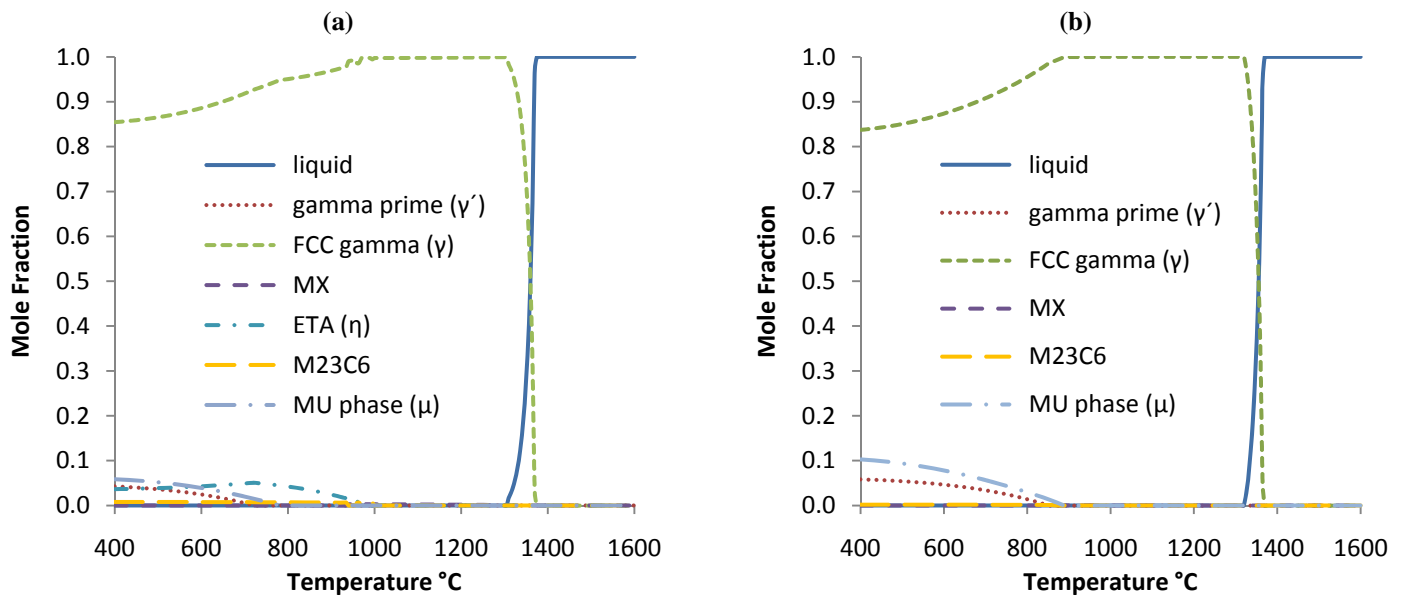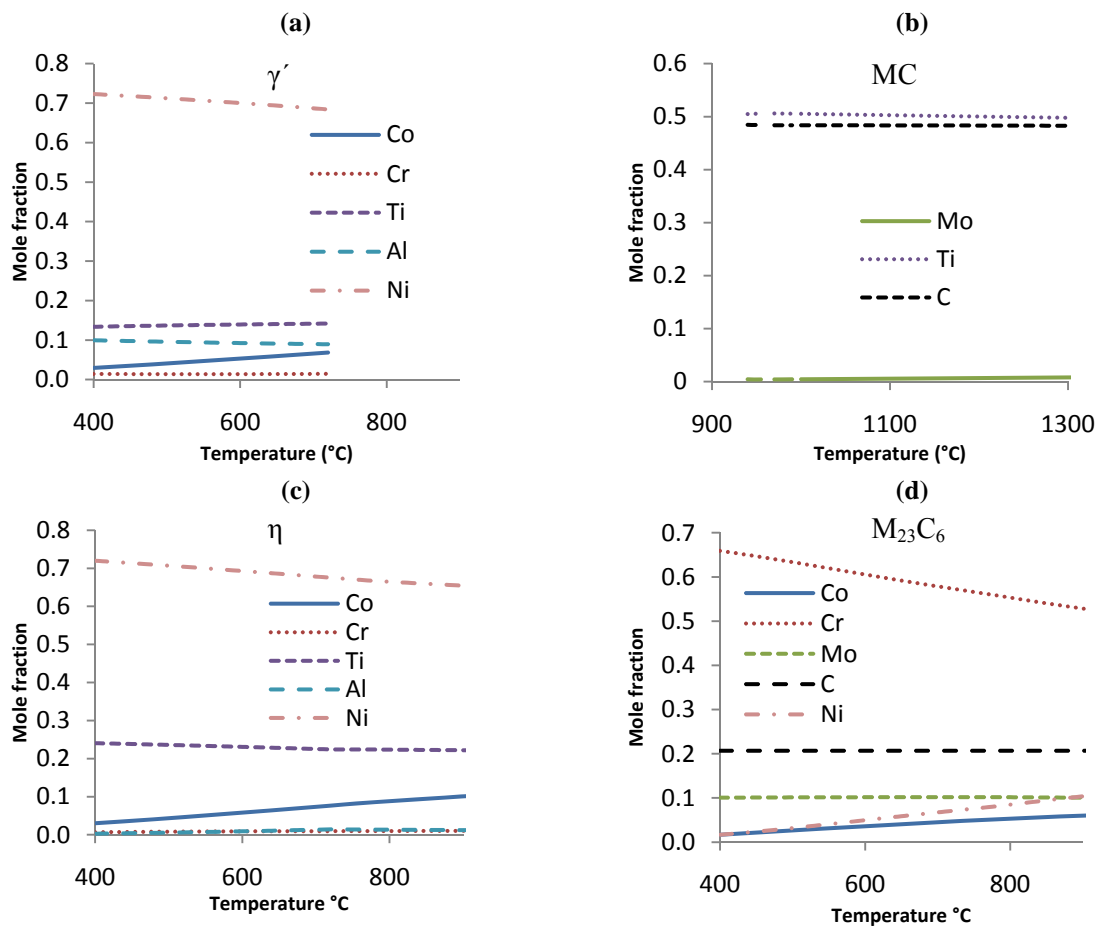

Figure 1: (a) Nimonic 263 predicted phases against temperature in equilibrium conditions, (b) predicted phases with Eta phase suspended from the calculations

In addition to predicting the phases present, the composition of each phase can also be calculated as a function of temperature, as shown in Figures 2(a – d).


Figure 2: Composition calculations for Nimonic 263: (a) γ´, (b) MC, (c) η and (d) $M_{23}C_6$ as a function of temperature

Figures 2(a – c) show that the compositions of the γ´, MX and η precipitates can be seen to be relatively consistent as a function of temperature. Figure 2(a) indicates that the γ´ phase is calculated to be a Ni-Ti-Al rich precipitate with small amounts of Co and Cr. Figure 2(b) shows the calculation for the MC phase which contains half Ti and half C with a small fraction of Mo. Figure 2(c) shows the Eta phase to be predicted to be Ni-Ti rich, with both elements decreasing slightly in favour of Co when temperature is increased. Figure 2(d) shows $M_{23}C_6$ to be a Cr rich phase, in which Cr decreases with temperature in favour of Ni and Co.

A small change was noticed between the Al contents (0.31-0.37 wt.%) in the bore and the outside diameter as mentioned in the experimental section. This was deemed important due to sensitivity of γ´ formation to the Ti-Al ratio in the alloy. Additional calculations (allowing for all phases) predicted that the difference in Al is likely to result in a small difference in the amount of γ´ in each region, with corresponding fractions of 0.015 and 0.019 predicted to form in the bore and outside diameter respectively.

3.2 Hardness as a function of temperature
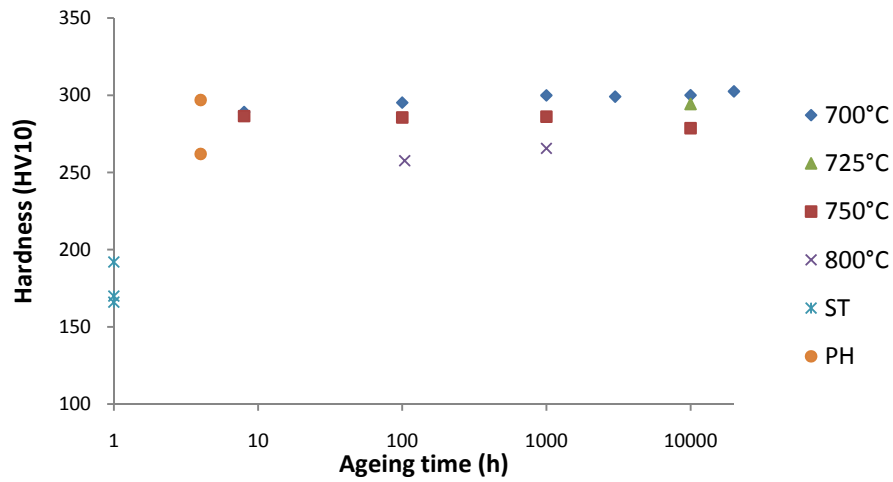
Figure 3: Plot showing the effect of ageing on hardness

The results from hardness testing are shown in Figure 3. The precipitation hardened samples can be seen to have hardened by approximately 100 HV from the solution treated sample. This increase was due to the precipitation of the gamma prime phase, which has formed during the 4 hour heat treatment at 800°C. The effect of ageing at 700°C can be seen to have very little effect on the hardness, even at the long term ageing heat treatment of 20,000 hours. Ageing at 725 and 750°C show unchanged hardness properties in short term ageing, although the 10,000 hour samples were seen to soften to 294 and 279 HV respectively, representing a small decrease in hardness when compared to the 700°C aged sample.

3.3 Grain size and distribution

Optical microscopy of the samples showed that there was a significant number of twins present with a bimodal grain size of large equiaxed grains and banded regions of smaller grains; an example optical micrograph is shown in Figure 4. The banded regions are thought to form during extrusion. Grain sizes were determined using a linear intercept method, and increased from 85 µm in the solution treated sample to 109 µm in the long term ageing treatment at 700°C representing a total increase of 24 µm, as shown in Figure 5.
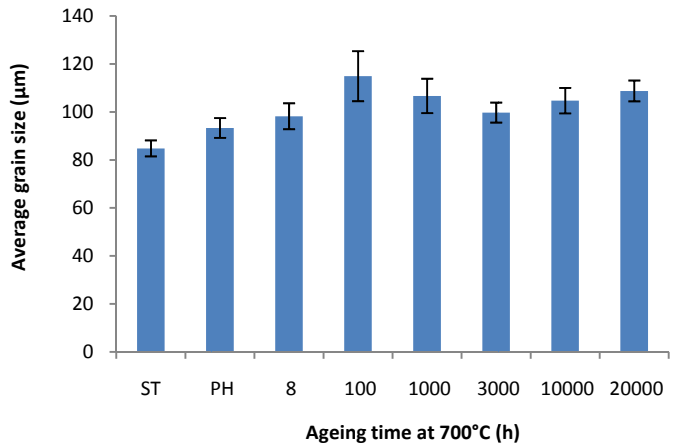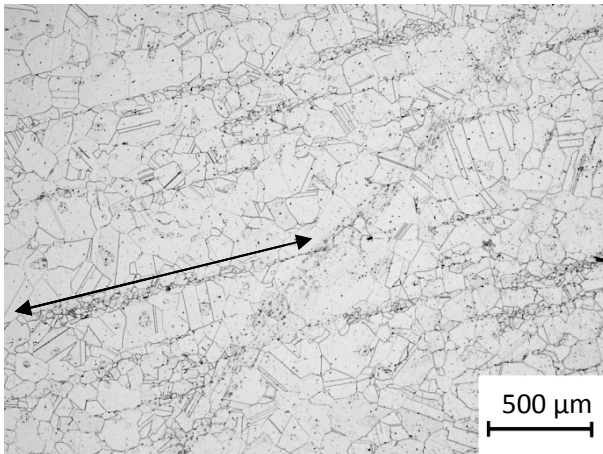
Figure 4: Optical image of solution treated sample showing the bimodal grain size distribution present in 263 (line highlighting one of the banded regions and its direction)

Figure 5: Plot indicating the change in average grain size with ageing at 700°C
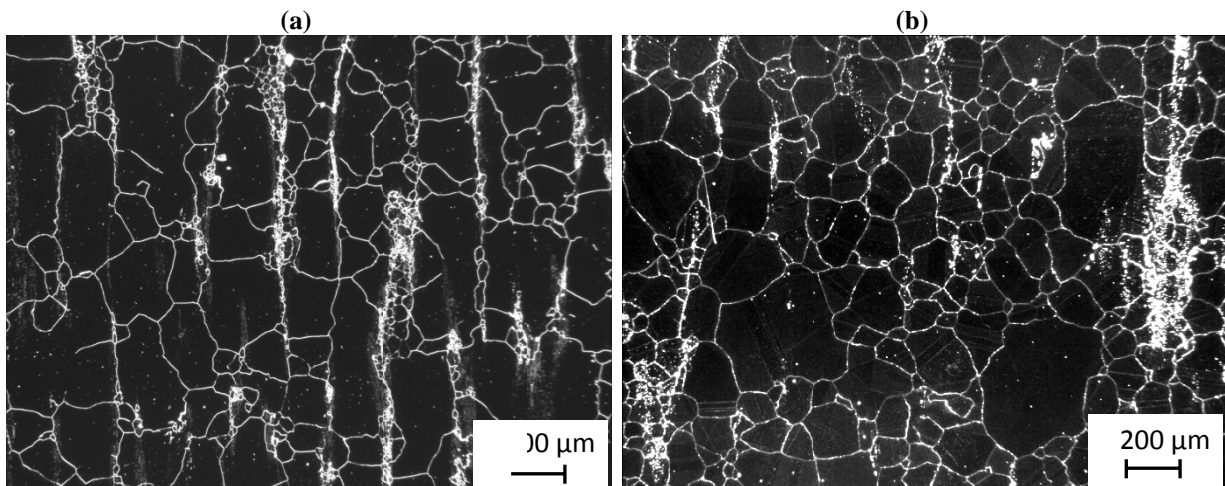
Figure 6: (a) Dark field image of sample having undergone standard heat treatment of 1150°C for 2h and 800°C for 4h, (b) Dark field image of sample having undergone standard heat treatment, then 20,000h of ageing at 700°C

Figures 6 (a) and (b) show dark field optical microscope images in which it can be seen that the banded regions are more visible and possible to quantify. The banded regions were then traced and analysed in terms of their area fraction using image analysis software. After analysis, a clear reduction in the area fraction of the banded regions between the precipitation hardened and the long term aged samples were noted, from 5 % in the precipitation hardened sample down to 2 % in the long term aged sample. Although a slight increase in the overall grain size was observed, the two dark field micrographs show that the bulk grain size is still large and little change has occurred. The reduction in area fraction of banded grains and the overall increase in bulk grain size suggest that coarsening of the banded regions may have occurred.

3.4 MX precipitation

Large precipitates were observed throughout the alloy, examples of which can be seen in Figures 7, 8 and 9. The precipitates can be characterised into three groups: large dark precipitates, lighter banded precipitates and bands of sub micron spherical precipitates. The large dark precipitates were observed to form individually and as stringers both in the matrix and along grain boundaries. Experimental observations indicated that these large, dark precipitates were present as both elongated and blocky morphologies at sizes up to 30 μm. EDX analysis of these precipitates confirmed them to be Ti rich with small amount of Mo, as shown in Table 3. The precipitates appearing lighter in contrast are present throughout the alloy, although predominantly concentrated along grain boundary positions and especially in the banded regions of smaller grains. The precipitates were observed to form as elongated precipitates aligned in one direction generally in sizes between 2 and 10 μm. EDX analysis of these precipitates confirmed them to be Ti-Mo rich as shown in Table 3. The submicron particles were observed to form in bands at close proximity to the lighter precipitates, and EDX analysis showed them to have the similar chemical compositions.

*Table 3: MX chemical composition*

Precipitate	Ti rich		Ti-Mo rich[*]	
	Ti (wt.%)	Mo (wt.%)	Ti (wt.%)	Mo (wt.%)
ST	98.3	1.7	61.7	38.3
PH	97.4	2.6	64.3	35.7
20,000h aged at 700°C	94.7	5.3	63.8	36.3

[*]*Composition for both lighter precipitates and submicron sized spherical precipitates*

The chemical compositions displayed in Table 3 are typical of MX precipitates: one Ti rich and the other Ti-Mo rich. The Ti rich precipitates appear darker in contrast to the Ti-Mo rich in both SE and backscatter modes making it possible to distinguish between the two without the use of EDX techniques. Imaging carried out in backscatter mode also offers a better contrast between precipitates and the matrix, which proved useful when carrying out any image analysis on the MX precipitates.

Figure 7 shows both the large, dark Ti rich and the lighter Ti-Mo rich phases, in addition to the associated EDX maps for elements: Mo, Ti, C and Ni. These maps clearly show that the

dark precipitates are titanium rich and the grey precipitates are rich in both titanium and molybdenum. Figure 8 shows an image and the corresponding EDX maps of a Ti-Mo rich precipitate and band of finely dispersed, spherical Ti-Mo rich precipitates. The area around the Ti-Mo rich precipitate can be seen to be denuded of submicron particles.
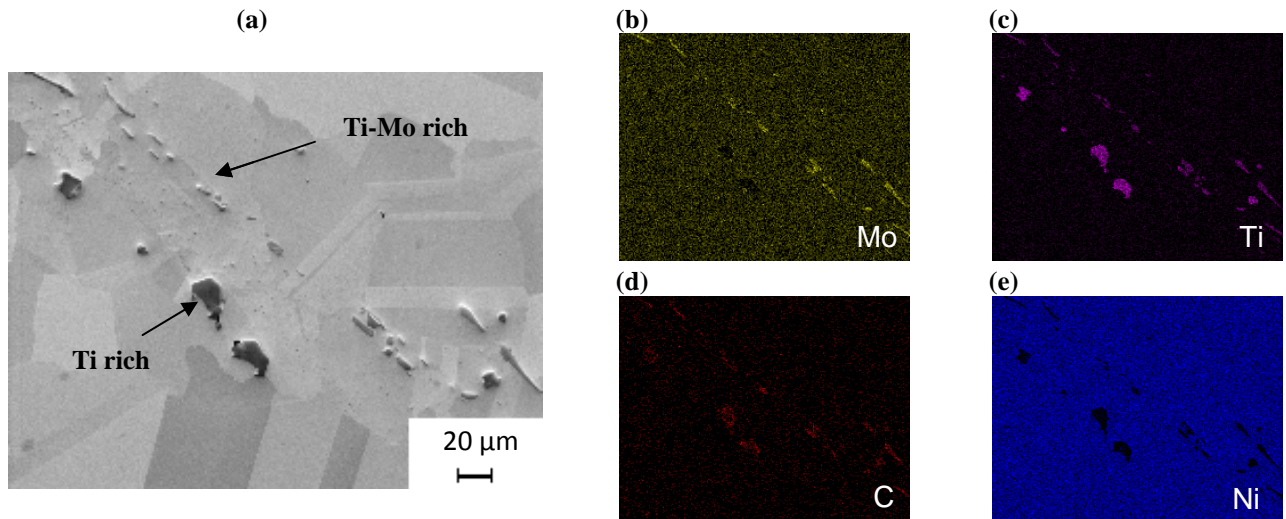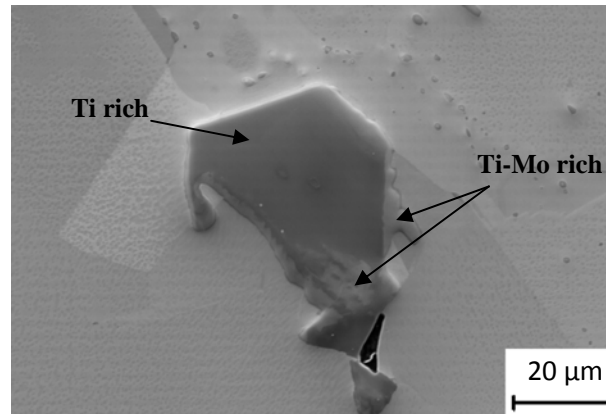

Figure 7: (a) An SE image of the solution treated sample showing both Ti rich and Ti-Mo rich MX precipitates, (b) Mo, (c) Ti, (d) C and (e) Ni EDX maps
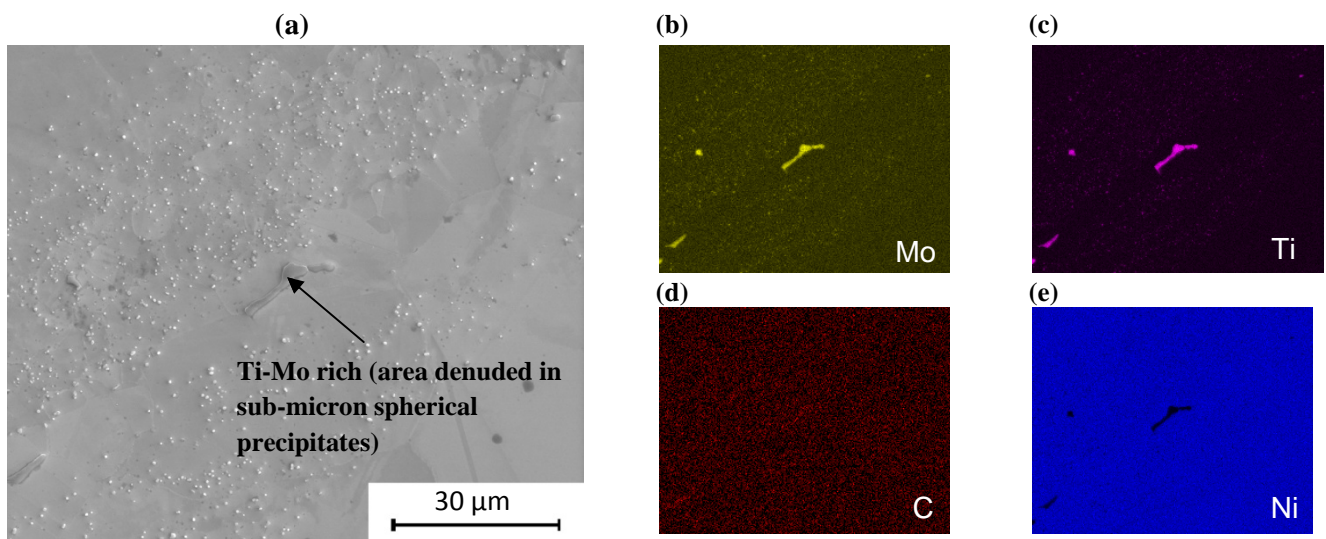
Figure 8: (a) A secondary electron image of the precipitation hardened sample showing a large Ti-Mo rich particle and a band of finely dispersed Ti-Mo rich spherical particles, (b) Mo EDS map, (c) Ti EDS map, (d) C EDS map and (e) Ni EDS map

As seen in Table 3, the chemical composition of both particle types were studied in samples subjected to different heat treatments. The variation in the Ti rich MX results show a small increase in Mo content from 1.7 wt.% in the solution treated sample to 5.3 wt.% in the long term aged sample. The Ti-Mo rich MX was found to stay at a relatively constant composition, with very little change observed. It should be noted that only one variant of MX, predominantly TiX, was predicted by the thermodynamic calculations, whereas a stable carbonitride appears to exist containing some Mo substituted for Ti.

It was noted that different compositions could be detected in the same precipitate depending on the placement of the spot. Further analysis showed that many of the larger Ti rich precipitates contained areas rich in molybdenum which exhibited a different contrast, as shown in Figure 9.


Figure 9: SE image of the solution treated sample showing the 'marbled' effect in MX precipitate as a result of Ti-Mo rich regions

The particle size and distribution of the bulk MX precipitates were determined using backscatter micrographs sampled at random from each specimen. The size and distribution of MX precipitates were calculated using image analysis software which determines the size of each precipitate, before grouping each precipitate into a certain size range e.g. 2 − 4 μm. Results indicated that the average MX size increases from 3.9 μm in the solution treated sample to 4.6 μm in the sample aged at $700^{o}C$ for 20,000 h, a resultant increase of 0.7 μm. The bulk MX particle size distribution also indicated that there were an increased number of smaller precipitates in the solution treated sample, however, overall there was very little change between the samples.
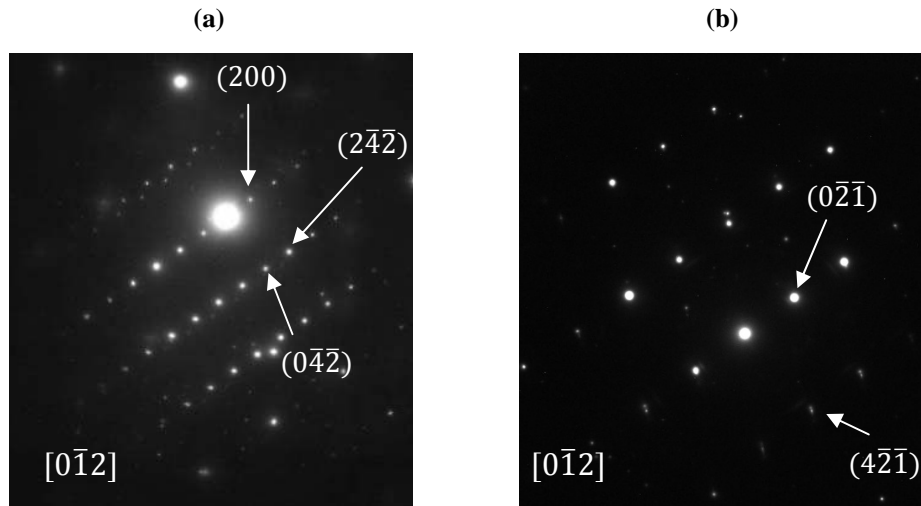
3.5 Grain boundary precipitates

The site-specific thin foils produced in the dual beam were analysed using the TEM. The same sample set of the solution treated, precipitation hardened and the long term aged, 20,000 h, specimen at $700^{o}C$ were examined. Samples were analysed to initially establish the presence of any grain boundary precipitates, and secondly to obtain information on their size and composition.

A number of samples in the solution treated condition were examined in this work, and the majority showed no grain boundary precipitation, as shown in Figure 10(a). However, one solution treated sample did present grain boundary precipitates of approximately 100 nm in size, possibly due to differences in cooling rate across the thick section pipe. The precipitation hardened samples contained grain boundary precipitates, at approximately 100 nm in size, as shown in Figure 10(b). Analysis of the long term aged sample at $700^{o}C$ shown in Figure 10(c) indicated the presence of larger grain boundary precipitates in the range 200 to 300 nm. Observations from analysis in the TEM therefore indicated that the grain boundary precipitates coarsened during ageing.
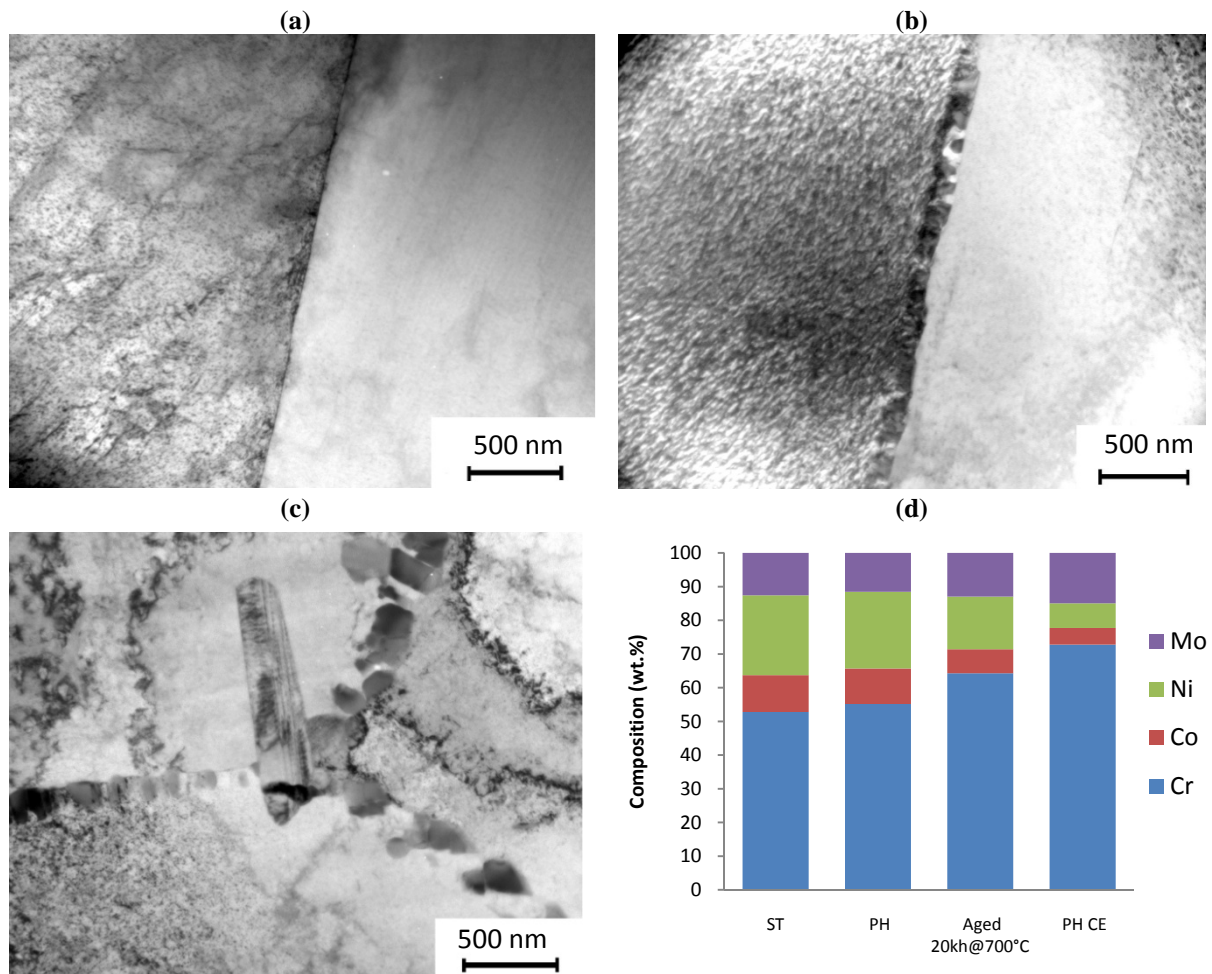
Figure 10: Transmission electron micrographs showing (a) Solution treated sample showing no GB precipitation, (b) Precipitation hardened samples showing continuous precipitation of GB particles, (c) Long term aged sample at 700°C showing both GB carbides and a large angular precipitate and (d)bar chart showing the compositional change in the GB precipitates for each sample

Elemental analysis using the EDX technique was carried out on the grain boundary precipitates present in the different samples, and the results are summarised in Figure 10(d). Analysis of the solution treated sample which did contain precipitates indicated them to be Cr, Ni, Mo and Co rich, with the chromium levels at approximately 53 wt.%. The precipitation hardened sample presented chemically similar precipitates with a slightly higher average chromium content of 56 wt.%. Elemental analysis of the long term aged sample showed further increases in chromium content of the grain boundary precipitates up to 64 wt.%. For comparison, the chemical composition measured from a grain boundary particle on a carbon extraction replica sample, rather than a thin foil, is also shown in Figure 10d. Chemical analysis therefore suggested that the Cr content of these particles increased slightly with increasing ageing time, although the possibility that this is related to the degree of beam overlap between the particle and the matrix reducing as the particles become larger cannot be ruled out.

Figure 11: Diffraction pattern from (a) grain boundary precipitate in the precipitation hardened sample, (b) larger, elongated angular precipitate in long term aged sample aged for 20,000 h at 700°C

Selected area electron diffraction was carried out in the TEM in order to identify the particles. The diffraction pattern shown in Figure 11a was consistent with the crystal structure (face centred cubic) and lattice parameter (10.621 Å) of $M_{23}C_6$. Therefore, from the chemical compositions, thermodynamic predictions and electron diffraction, the grain boundary particles were identified as $M_{23}C_6$.

In addition to the grain boundary precipitates, the presence of isolated large, elongated angular precipitates about 1 μm in length, mainly associated with the grain boundaries, was noted in the sample aged for 20,000 h at 700°C. EDX analysis indicated that the composition of these particles was ~69 wt.% Ni and 14 wt.% Ti with small amounts of Al, Cr, Co and Mo substitution. Selected area electron diffraction was also carried out on these particle types, as shown in Figure 11b. The combination of particle chemistry and crystallographic information and thermodynamic calculations indicated that these particles were the η phase, which was therefore able to form after very long ageing times within the matrix. It has been suggested[7] that eta can be detrimental to the mechanical strength of Nimonic 263, and can form at the expense of gamma prime. It was noted that there is a precipitate denuded zone around the η phase particles, consistent with a synergistic relationship between η and gamma prime.

13

3.6 Gamma prime precipitation and coarsening

Samples were etched using Fry's reagent to reveal the presence of very fine precipitates within the bulk of the matrix of the different samples, which were then analysed using the FEGSEM to quantify both their size and distribution. Representative micrographs showing fine scale precipitation are shown in Figures 12a–e. The strengthening precipitate present within the matrix of the alloy is expected to be gamma prime[5], with a composition from thermodynamic predictions similar to the stoichiometry $Ni_3(Al,Ti)$. No gamma prime
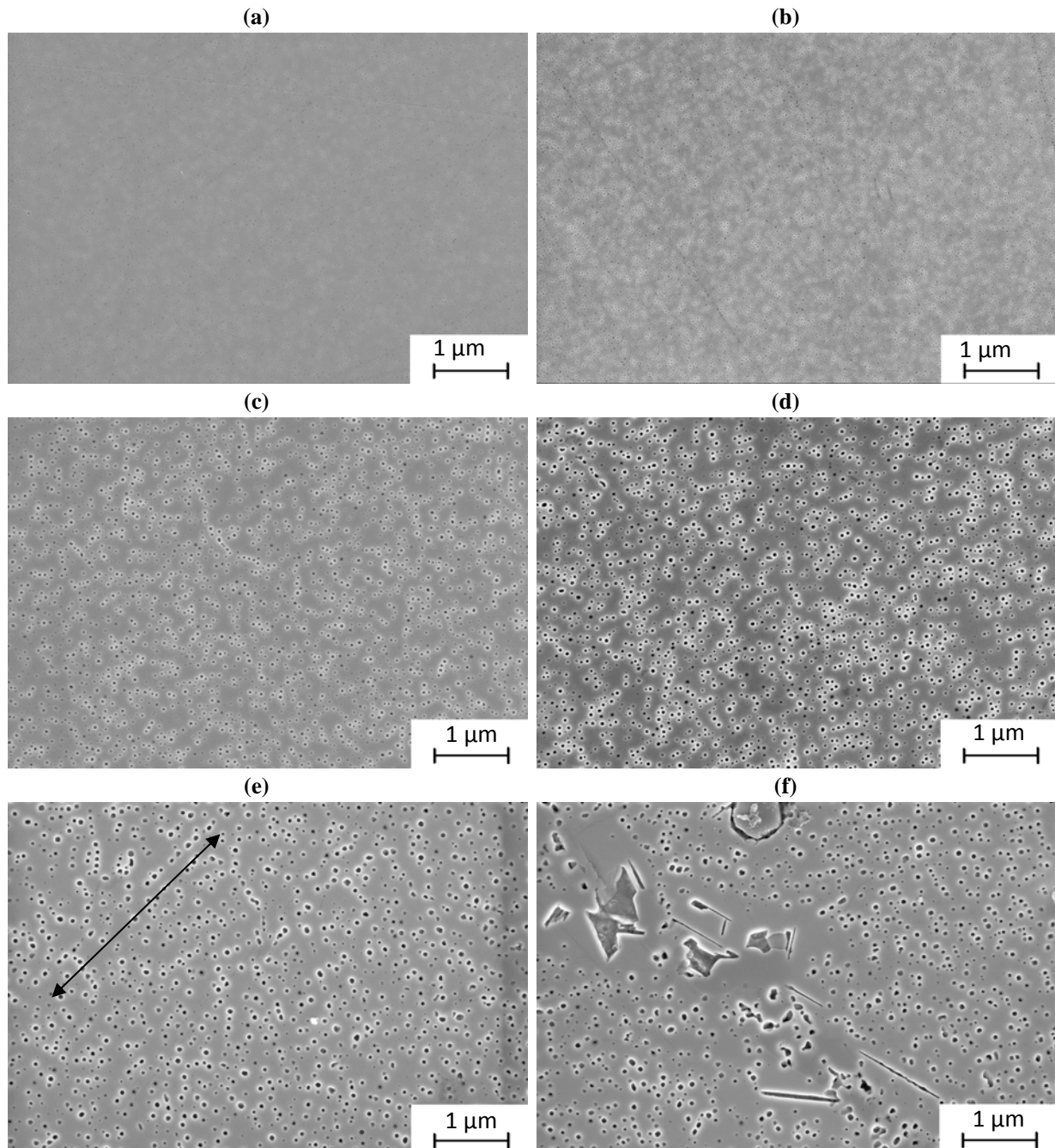
Figure 12: Micrographs showing gamma prime taken at the same magnification in (a) Precipitation hardened sample, (b) Aged at 700°C for 100h, (c) Aged at 700°C for 3000h, (d) Aged at 700°C for 10000h, (e) Aged at 700°C for 20000h and (f) Aged at 700°C for 20000h showing extensive precipitation along the grain boundaries, in addition to the gamma prime particles within the matrix

precipitates were observed in the solution treated sample, or if present they were too small to be detected. However, fine precipitates, assumed to be gamma prime, were detected in the precipitation hardened sample and samples aged at 700°C. The micrographs presented in Figure 12 show that there is significant coarsening of these particles with increasing ageing time.

The coarsening behaviour of the fine particle distribution has been quantified by investigating the average size and distribution of the gamma prime precipitates in each sample. Image analysis software was used to analyse ~10 micrographs from each sample condition. A significant number of particles were considered in each sample condition, typically over 10,000, ensuring good statistical significance in the measurements. The results for the short term aged samples, displayed in Figure 13(a) as the number of particles within a particular size range, show a relatively narrow distribution, as would be expected for newly formed precipitates. The average particle sizes in the short term aged samples were: 9.8 nm in the precipitation hardened sample, 11.4 nm after 8 h, 11.5 nm after 100 h and 15.2 nm after ageing for 1000 hours.
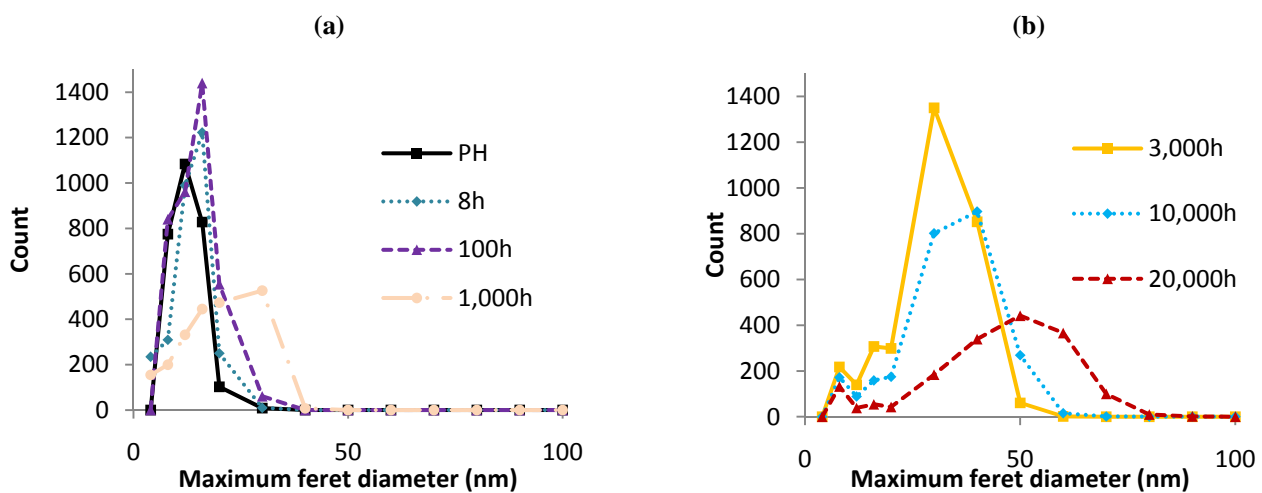
(a)   **(b)**

Figure 13: Particle size distribution of (a) short term aged samples (b) Long term aged samples

Figure 13b shows the particle size distribution of the long term aged samples. As expected, these distributions are much broader than the short term ageing heat treatments. The average particle sizes in the long term aged samples are: 24.6 nm in the 3000 hour aged, 28.2 nm in the 10000 hour aged and 39.2 nm in the 20000 hour aged. The average particle sizes for all samples are plotted in Figure 14a as a function of ageing time at 700°C. Figure 14b further plots the average particle size as a function of the cubic root of time for comparison with standard particle coarsening theory. It can be seen that an approximately linear fit is indeed observed, and the steeper gradient at 750°C indicating a faster rate of coarsening at the higher temperature.
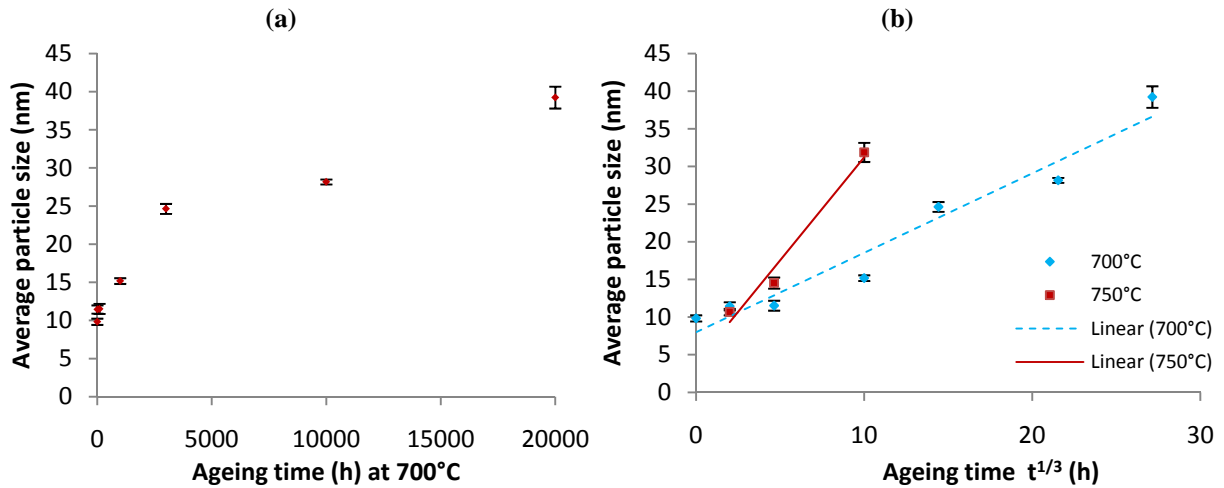
Figure 14: (a) Average particle size against ageing time for 700°C sample set, (b) average particle size against ageing time$^{1/3}$ for both 700 and 750°C sample set

4. Conclusions

Microstructural evolution in thick section Nimonic 263 has been studied using a number of analytical techniques, with particular focus on long term ageing at 700°C.

Hardness measurements showed a large increase of approximately 100 HV after solution treatment in the precipitation hardening heat treatment, primarily attributable to the precipitation of fine γ′. Further changes in hardness on long term ageing at temperatures ranging from 700°C to 800°C were relatively small, although there was some apparent softening with increasing thermal exposure. The γ′ precipitates were observed to coarsen as a function of thermal exposure, and quantification of the evolution of the particle size distribution showed good agreement with standard particle coarsening theory.

Significant banding was present in the microstructure with a bimodal grain size distribution comprising fine grains within the banded regions. There was little overall change in the bulk grain size, although the banded regions were noted to coarsen after long term ageing.

The alloy contained two different types of larger MX precipitates; one Ti rich and the other Ti-Mo rich. These precipitates were observed to coarsen very slowly when aged at 700°C, only increasing by 0.7 μm after 20,000 hours. Some individual particles were found to contain distinct regions which were rich in each of the two compositions observed.

The grain boundaries in the samples after solution treatment only remained particle-free, with precipitation occurring during the initial precipitation hardening heat treatment. Grain boundary precipitates were identified as the Cr-rich $M_{23}C_6$ phase, and were also observed to coarsen with long term ageing. After ageing for 20,000 hours ageing at 700°C, large, angular, individual particles were detected in the vicinity of the grain boundaries, which were identified as the η phase. The influence of the precipitation of this phase on the long term creep properties of the material requires further investigation.

16

5. Acknowledgements

6. References

[1] Allen DJ, Barrie M, Fry A, Hannis J, McColvin G, Oakey J, et al. Materials UK Energy Review 2007: Fossil-fuelled power generation. 2007.

[2] W. Betteridge, J. Heslop. The Nimonic Alloys and other nickel-base high temperature alloys. 2nd ed. Great Britain: Edward Arnold Limited; 1974.

[3] Wang WZ, Hong HU, Kim IS, Choi BG, Jeong HW, Kim MY, et al. Influence of gamma' and grain boundary carbide on tensile fracture behaviors of Nimonic 263. Materials Science and Engineering A-Structural Materials Properties Microstructure and Processing 2009;523(1-2):242-245.

[4] Special Metals: Nimonic alloy 263. 2004;SMC-054.

[5] Zhao JC, Ravikumar V, Beltran AM. Phase precipitation and phase stability in Nimonic 263. Metallurgical and Materials Transactions A-Physical Metallurgy and Materials Science 2001;32(6):1271-1282.

[6] Murthy GVS, Anish K, Sridhar G, Jayakumar T, Ghosh RN. Characterization of Precipitation Behavior in Nimonic 263 by Ultrasonic Velocity Measurements. Review of Progress in Quantitative Nondestructive Evaluation, Vols 28a and 28b 2009;1096:1252-1258.

[7] Sims CT, Norman S. Stoloff, William C. Hagel. Superalloys II High-temperature materials for aerospace and industrial power. 1st ed. United States of America: John Wiley & Sons; 1987.

[8] Davies RH, Dinsdale AT, Gisby JA, Robinson JAJ, Martin SM. MTDATA - Thermodynamics and Phase Equilibrium Software from the National Physical Laboratory. 2002:229-271.

[9] N. Saunders: Proc. 8th Int. Symp. on 'Superalloys (Superalloys 1996)', (ed. R. D. Kissinger et al.), 101–110; 1996, Warrendale, PA, The Minerals, Metals & Materials Society, Seven Springs.